




A simulation study of temperature effects on performance parameters of silicon heterojunction solar cells with different ITO/a-Si:H selective contacts

Jošt Balent*, Marko Topič, Janez Krč

University of Ljubljana, Faculty of Electrical Engineering, Tržaška cesta 25, 1000 Ljubljana, Slovenia

Article info

Article history:

Received 6 Nov. 2021

Received in revised form 4 Jan. 2022

Accepted 9 Jan. 2022

Available on-line 24 Feb. 2022

Keywords:

Heterojunction; photovoltaics; simulation; temperature; tunnelling.

Abstract

Effects of temperature variation on the performance of silicon heterojunction solar cells are studied using opto-electrical simulations. It is shown that the low-temperature cell efficiency is determined by the fill factor, while at high temperatures it depends on the open-circuit voltage. Simulations revealed that the low-temperature drop in the fill factor is caused by poor tunnelling, in particular at the ITO/p-a-Si:H heterojunction. The authors link this drop in fill factor to a low maximum-power-point voltage and show how poor tunnelling is reflected in the charge redistribution determining the device voltage. The effect of the contact work function on temperature behaviour of efficiency by varying the electron affinity of ITO layers has been demonstrated. It was also demonstrated that increasing the electron affinity of ITO on the p-side minimises the work function mismatch, leading to significant improvements in efficiency, especially at low temperatures, while optimisation on the n-side results in marginal improvements over the entire temperature range. In addition to the cumulative effects of the temperature-dependent parameters, their individual contributions to the efficiency were also investigated. Moreover, it was presented that the thermal energy (kT) determines the efficiency temperature behaviour, while other parameters play only a minor role. This paper shows how temperature variations affect device performance parameters.

1. Introduction

The need for renewable and affordable energy sparked the ever-growing market and development of photovoltaics (PVs). Continuous progress has been made in wafer-based and thin-film PV technologies in terms of increasing energy conversion efficiencies [1], long term reliability, and lowering solar cell and PV system costs [2]. In case of mono- and multi-crystalline silicon wafer-based solar cells, various architectures such as passivated emitter and rear contact (PERC), passivated emitter and rear locally diffused (PERL), passivated emitter and rear totally diffused (PERT) [3], tunnelling oxide passivated contact (TopCon) [4], and others are researched and transferred to

the industrial level [2]. In the case of thin-film PVs, besides cadmium-telluride (CdTe) and copper-indium-gallium-diselenide (CIGS), perovskite-based solar cells have gained a lot of attention in recent years. [5]. Moreover, wafer-based and thin-film technologies are combined in order to use the advantages of both technologies resulting in high-efficiency, potentially low-cost, solar cell devices. A representative of such an approach is a silicon heterojunction (SHJ) solar cell which is also in the research focus of this paper. The tandem and multi-junction solar cells can be used to lower thermalization losses of single-junction devices to reach higher conversion efficiencies [6]. The tandem perovskite/silicon solar cell recently reached a record-breaking efficiency of 29.8% by combining a thin-film and wafer-based solar cell into a single device [7]. Among the various solar cell technologies, crystalline-

*Corresponding author at: jost.balent@fe.uni-lj.si

silicon (c-Si) based solar cell architectures currently account for ~95 % of the total market share [2]. Among the state-of-the-art structures, the above mentioned SHJ solar cells use the advantages of the established wafer-based (c-Si) and thin-film (hydrogenated amorphous silicon a-Si:H) technologies. The world record efficiency among Si cells is currently set at 26.7 % by the SHJ structure combined with an interdigitated-back-contact (IBC) pattern [1, 8].

Understanding the physical mechanisms that determine the external electrical parameters of a solar cell is critical to achieve efficiencies at the edge of the theoretical limit (~30 % for single-junction silicon devices) [9]. Numerical simulations play an important role in this respect, as they do not only offer a detailed look into the internal, usually immeasurable, quantities of a solar cell, but also expedite the device design and optimization process. Solar cells are usually characterised and optimized for STC, where the cell temperature (T) is set to 25 °C [10]. However, the cells in the field typically operate at different illumination, wind, and temperature conditions [11] which highlights the importance of studying and optimizing the device performance outside the STC conditions.

In this paper, a simulation analysis of the SHJ cell performance under different temperatures, applying different indium-tin-oxide (ITO)/a-Si:H contacts was carried out. In particular, ITOs with different work functions were applied and temperature behaviour of the cell was monitored. By employing numerical modelling with Sentaurus, a TCAD simulation tool [12], a detailed study was performed which explained the impacts of temperature on the solar cell performance parameters (efficiency – Eff , fill factor – FF , short-circuit current – J_{sc} , and open-circuit voltage – V_{oc}) of a SHJ solar cell. In general, crystalline silicon solar cells are more sensitive to temperature variations (higher temperature coefficients) when compared to their thin-film amorphous or nano-crystalline silicon counterparts [13]. It is known that SHJ cells, combining the two technologies, exhibit lower temperature coefficients than regular crystalline silicon solar cells and higher ones than thin-film a-Si:H cells [14].

In the presented paper, the SHJ solar cell structure, including ITOs that were modelled as full semiconductor layers, is considered together with the accompanying tunnelling effects (direct, band-to-band, trap-assisted), since it was shown in our previous publication that ITO layers should be included in the analysis in order to properly describe and explain the device behaviour [15].

Recent simulation and experimental studies of temperature effects on the SHJ solar cell performance showed that efficiency is deteriorated at both temperatures below and above the STC temperature (25 °C) [11, 16–20]. At low temperatures the reduction of efficiency was mostly attributed to lowering of the FF , due to the ITO/a-Si:H heterojunction (and their work function mismatch) [16, 18], whereas at temperatures above STC it was attributed to lowering of the V_{oc} [11, 20].

In this work, the authors aim to further expand upon the aforementioned studies, by explaining the observed trends in more detail. First, cells with realistic ITO/a-Si:H selective contacts were compared to cells that use idealized ohmic contacts at different temperatures to determine the effects on the ITO/a-Si:H and a-Si:H/c-Si heterojunctions and their influence on the performance parameters.

Simulations of the structures with different ITO work functions (on the p- and n-side of the device) were performed which showed their influence on the temperature dependency. Next, a sensitivity analysis of the selected temperature-dependent materials parameters was carried out: band gap (E_G), effective density of states of the conduction (E_C), and valence (E_V) bands, mobility (μ), and the thermal energy (kT) (where k is the Boltzmann constant) to give quantitative indications of which parameters affect the temperature behaviour of the SHJ cell the most. This study contributes to a better understanding of the cumulative temperature dependency behaviour of the device and opens the scope for further optimizations. Finally, explaining the related effects on the solar cell operating under the maximum-power-point (MPP) condition will remain the focus of the authors, as this is the most typical scenario in real-world solar-cell operation and has not been addressed in such a direct manner in previous publications.

2. Device structure and models

2.1. Simulated SHJ structure

The analysis was based on the following SHJ structure (see Fig. 1): ITO front cathode (70 nm), p-a-Si:H-doped layer (10 nm), i-a-Si:H passivation layer (5 nm), n-c-Si bulk absorber (150 μm) with defective interface regions at both i-a-Si:H/n-c-Si interfaces (both 2 nm thick), i-a-Si:H passivation layer (5 nm), n-a-Si:H-doped layer (10 nm), and rear anode ITO (100 nm)/Al contact layer (500 nm).

The layer stacks ITO/p-a-Si:H and ITO/n-a-Si:H allow for a selective extraction and collection of holes and electrons generated by light in the n-c-Si bulk. The thin i-a-Si:H layers are used to passivate the surface on both sides of the n-c-Si bulk which decreases the surface recombination rate of carriers. The energy band diagram of the device in thermal equilibrium at 300 K (26.85 °C) is presented in Fig. 1(b), where the vertical black dashed lines segment the structure to distinguish between the individual layers (regions). The heterointerfaces between the ITO/a-Si:H and i-a-Si:H/n-c-Si layers and the energy barriers due to the band offsets are clearly visible. The energy band diagram will be addressed in the later discussion.

2.2. Optical and electrical model

The optical generation distribution in the SHJ was calculated using a SunShine[®] simulator [21], taking into account both coherent and incoherent nature of light in the thin and thick layers, respectively. Light scattering and anti-reflection effects at the front and at the rear side of the device were applied to the device interfaces, resulting in a current density of over 40 mA/cm² for the AM1.5g solar spectrum [22]. Wavelength-dependent realistic complex refractive indices of all layers were considered in simulations [23–25]. The investigation was not focused on a detailed optical analysis of the device in this paper, however, we considered the temperature effect of band gap narrowing of silicon layers on optical charge carrier generation.

The Sentaurus TCAD software package [12] was used for electrical simulations which had been previously used

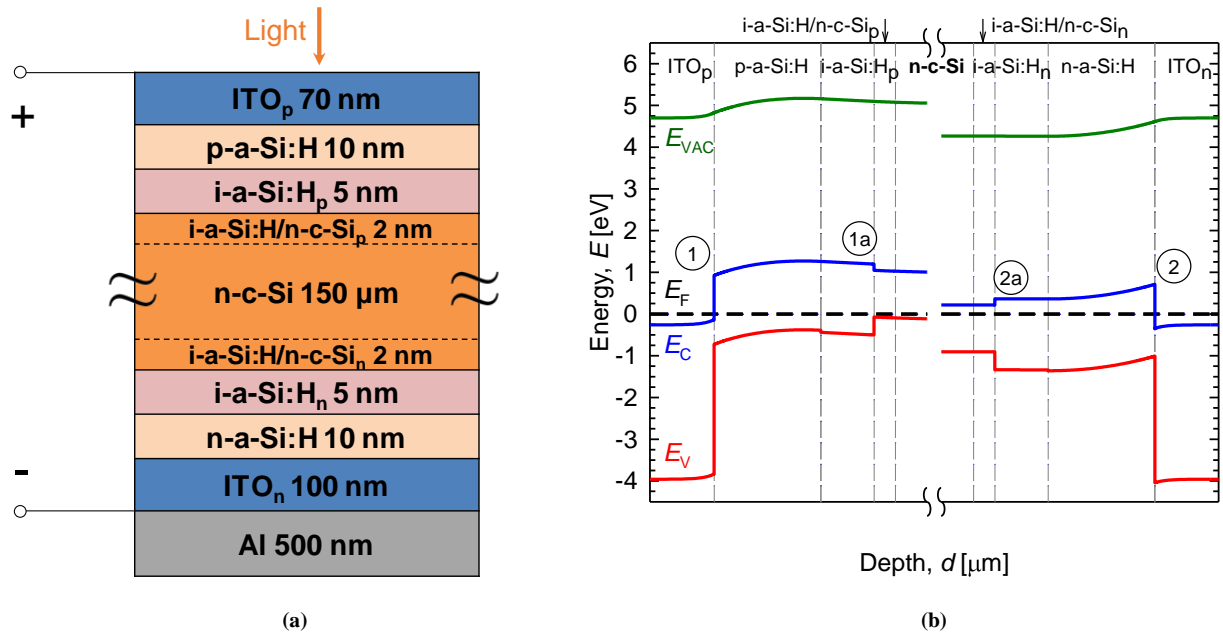


Fig.1. Schematic of the SHJ solar cell structure (a) and the energy band diagram in thermal equilibrium at 300 K (26.85 °C) (b). The labels E_C , E_V , E_F , and E_{VAC} stand for the conduction band, the valence band, the Fermi level energy, and the vacuum level energy, respectively. Subscripts p and n denote the side to which the layer belongs to. The circled numbers 1 and 2 mark the ITO/a-Si:H interfaces and 1a and 2a the i-a-Si:H/n-c-Si interfaces on their respective sides. Please note that the band diagram is zoomed-in at the front and rear parts of the device and that only a small part of the thick n-c-Si absorber is shown.

and validated for simulation of such solar cell structures [26–29]. An ohmic contact was assumed at the rear (ITO/Al) interface. No front metal grid was taken into account in simulations. The interfaces were geometrically regarded to be flat in electrical simulations, taking into consideration the increasing defect concentrations on n-c-Si interface areas described earlier.

Since the influence of heat gradients along the simulated structure was not explored in this work, the drift-diffusion model was used to solve the Poisson’s equation coupled with the continuity equations for charge concentrations within the solar cell structure. This model is limited to isothermal simulations in Sentaurus TCAD, consequently the temperature was kept at the same in all layers during temperature variations.

Fermi-Dirac statistics were used in all layers of the structure to obtain accurate results for charge distributions also in the heavily doped layers (ITO, p-a-Si:H and n-a-Si:H). Modelling of the charge recombination in the n-c-Si bulk included both, Auger and radiative mechanisms in the form first used by Richter *et al.* [30], and the Shockley-read-hall (SRH) mechanism, implemented as

lifetime of minority carriers (10 ms in the n-c-Si layer). In a-Si:H layers, defect states were presented by valence (donor-like) and conduction band (acceptor-like) tail states and dangling bond states. The amphoteric nature of dangling bond states was approximated by two Gaussian functions, where one is considered positively charged when unoccupied by an electron (+/0) and neutral otherwise, while the other is considered neutral when vacant and negatively charged when occupied by an electron (0/-). The ITO layers were assumed to be lossless in terms of Auger, radiative, and SRH recombination in this work. Transport through the i-a-Si:H/n-c-Si and ITO/a-Si:H interfaces was described by thermionic emission (TE) and band-to-band (BBT) tunnelling, trap-assisted tunnelling (TAT), and direct tunnelling (DT) mechanisms. The Poole-Frenkel effect, that describes the electric field dependence of emission on trap states, was also considered in this work. The tunnelling models used are non-local and take into account the variation of band-edge energies, as well as the variation of the electric field along the structure which guarantees zero current at thermal equilibrium (this does not apply to the simpler so-called local models).

Table 1.
Parameters for the reference cell at 300 K (26.85 °C).

Symbol	Quantity	n-c-Si	p-a-Si:H	i-a-Si:H	n-a-Si:H	ITO
χ (eV)	Electron affinity	4.05	3.9	3.9	3.9	4.96
E_G (eV)	Band gap energy	1.12	1.65	1.70	1.72	3.7
N_D/N_A (cm ⁻³)	Effective doping conc.	2·10 ¹⁵ /0	0/2·10 ¹⁹	2.2·10 ¹⁵ /0	1.5·10 ¹⁹ /0	1·10 ²⁰ /0
E_A (meV)	Activation energy	246	300	545	200	-260 ^a
N_C/N_V (cm ⁻³)	Effective density of states	2.8·10 ¹⁹ /3.1·10 ¹⁹	2·10 ²⁰ /2·10 ²⁰	2·10 ²⁰ /2·10 ²⁰	2·10 ²⁰ /2·10 ²⁰	4.12·10 ¹⁸ /1.17·10 ¹⁹
μ_e/μ_h (cm ² /Vs)	Mobility	1342/452	10/1	10/1	10/1	50/30

^a ITO is modelled as a degenerately doped semiconductor layer and activation energy is therefore negative.

Electrical simulations of the SHJ device were carried out in two dimensions, but since the topic under investigation is one-dimensional, the findings have been translated and presented as a function of a single dimension (structure depth). The electrical model with experimental input parameters reported in different publications [28, 29, 31] was established and calibrated. Selection of the most important parameters is presented in Table 1. For details of the simulated structures and other input parameters corresponding to the reference temperature of 300 K (26.85 °C) can be found in our previous publication [15].

2.3. Temperature models

Temperature dependent free electron (n) and hole (p) concentrations have been considered by the known equations (1), (2), and (3) [5]:

$$n = N_C(T) \cdot \mathcal{F}_{1/2} \left(\frac{E_{F,n} - E_C}{kT} \right), \quad (1)$$

$$p = N_V(T) \cdot \mathcal{F}_{1/2} \left(\frac{E_V - E_{F,p}}{kT} \right), \quad (2)$$

$$N_{C,V}(T) = N_{C,V}(T_0) \cdot \left(\frac{T}{300 \text{ K}} \right)^{\frac{3}{2}}, \quad (3)$$

where $N_{C,V}(T)$ presents the temperature-dependant effective density of states of the conduction and valence bands, respectively, and the kT product is the thermal energy. In equation (3) T_0 is the reference temperature (300 K or 26.85 °C in this case), and $N_{C,V}(T_0)$ presents the reference values (see Table 1). This dependency was considered for the silicon-based layers only, whereas for the ITO, the N_C and N_V were not varied with temperature in this work and were kept at their reference values (see Table 1). The dependency of thermal energy on T was considered in all layers, including ITOs.

Great care was taken when selecting the appropriate temperature-independent doping concentrations for the doped layers in order to obtain realistic activation energies (see Table 1).

The temperature dependency of the diffusivity $D(T)$ and the mobility $\mu(T)$ (related by the Einstein's relation) of free particles is given by equations (4) and (5):

$$D_{n,p}(T) = \mu_{n,p}(T) \cdot \frac{kT}{q}, \quad (4)$$

$$\mu_{n,p}(T) = \mu_{n,p}(T_0) \cdot \left(\frac{T}{300 \text{ K}} \right)^{-\xi_{n,p}}, \quad (5)$$

where the subscripts n and p stand for the electrons and holes, respectively. Note that diffusivity was temperature-dependant in all layers due to the thermal energy (kT) variation. For mobility calculations (5), the parameter ξ was set to 2.5 for electrons and 2.2 for holes in both c-Si [32] and a-Si:H layers. The high mobility values in ITO layers were kept as temperature independent. The mobility values at $T_0 = 300 \text{ K}$ (26.85 °C) are given in Table 1.

Next, the temperature dependency of the band gap (E_G) and electron affinity (χ) in c-Si and a-Si:H was modelled by the following relations [33]:

$$E_G(T) = E_G(T_0) + \frac{\alpha T_0^2}{\beta + T_0} - \frac{\alpha T^2}{\beta + T}, \quad (6)$$

$$\chi(T) = \chi(T_0) - \frac{1}{2} \left(\frac{\alpha T_0^2}{\beta + T_0} + \frac{\alpha T^2}{\beta + T} \right), \quad (7)$$

where $\alpha = 0.473 \text{ meV/K}$ and $\beta = 636 \text{ K}$ for n-c-Si [33], and $\alpha = 0.63 \text{ meV/K}$ and $\beta = 0 \text{ K}$ for a-Si:H [34]. It should be noted that the band gap and electron affinity change at the same time in such a way that the conduction and valence band offsets are changed equally. The band gap energy and electron affinity of the ITO layers were temperature-independent in our simulations. See Table 1 for the reference values of band gap and electron affinity for all the layers.

Additionally, it was taken into account that changes in the band gap energy also influence the optical absorption and consequently the generation of free carriers by recalculating the absorption (α) coefficients for each wavelength for c-Si and a-Si:H layers at each temperature for the optical carrier generation calculations. The Tauc plot was used for modification of the absorption coefficients based on the change of E_G for a-Si:H [35] and c-Si [36] layers. The E_G of ITO layers was not changed in this manner, since the optical generation in ITO was considered to be negligible due to its high band gap energy.

No explicit temperature models of other material parameters (such as capture cross-sections, tunnelling mass, etc.) were included and they were kept at their baseline values during this analysis [15].

3. Results

3.1. Analysis of temperature effects for ideal ohmic and realistic ITO contacts

As the first step, opto-electrical simulations of the SHJ cell with the specified input parameters (Table 1) and their temperature dependencies in the temperature range from -20 °C to 80 °C were performed. All temperature models from equations (1)–(7) were applied, as well as the temperature dependent optical generation model.

To indicate the role of the ITO/a-Si:H contacts on the temperature-dependent behaviour of the SHJ cell, the analysis was performed first on the so-called ideal ohmic case (lines with the white circle markers in Fig. 2) where ideal ohmic boundary conditions were applied to the borders of p-a-Si:H and n-a-Si:H layers instead of ITO layers. Then, the cell with ITO contacts was simulated (as in all further simulations). Since tunnelling was considered for all hetero-interfaces (ITO/p-a-Si:H, ITO/n-a-Si:H and i-a-Si:H/n-c-Si on p and n-sides of the device), tunnelling through the i-a-Si/n-c-Si hetero-barriers in the ideal ohmic case was also included.

The results of simulations (efficiency – Eff , fill factor – FF , short-circuit current density – J_{SC} , and open-circuit voltage – V_{OC}) as a function of the solar cell temperature are presented in Fig. 2(a)–(d), respectively.

First, it can be observed that all external parameters are better (larger) for the cell where an ideal ohmic contact was assumed on both sides of the device (white circles) throughout the entire temperature range (-20 °C – 80 °C) compared to the realistic case with ITO contacts (black circles).

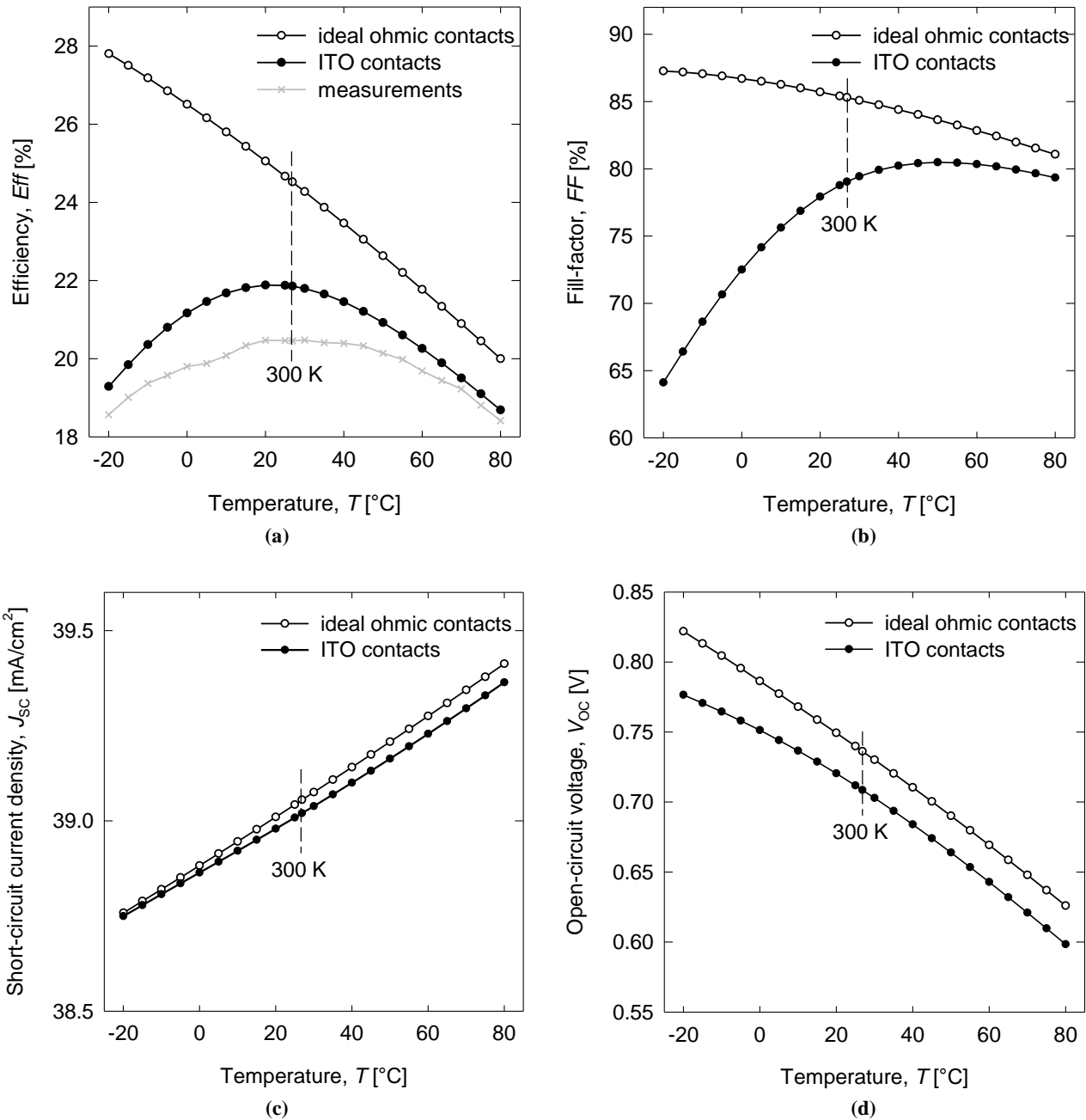


Fig. 2. Efficiency (a), fill factor (b), short-circuit current (c), and open-circuit voltage of the cell (d) for ideal ohmic contacts (open symbols) and ITO contacts (at p- and n-side in full symbols) as functions of temperature. Circles represent actual simulation points (which also refers to other graphs). The grey line with cross symbols in (a) presents measurements of the SHJ cell taken from Refs. 32 and 33.

Focusing first on the efficiency [Fig. 2(a)] for the ideal ohmic case (white circles), it was noticed that it decreases linearly with an increasing temperature over the entire temperature range, while in the ITO contact case (black circles) a curve with a clear maximum can be observed. In the analysed case, this maximum is located at a relatively high temperature of around 20 °C and reaches ~21.9%. The values of efficiency at $T = -20$ °C and 80 °C are 19.3% and 18.7%, respectively. The difference between the ideal ohmic case and ITO contact case will be addressed in the discussion section, as well as all the other effects noted in this section.

Let us stress here that the presented results are in accordance with experimental measurements published by other researchers [37–39]. They reported that the

temperature of the peak position may vary depending on the SHJ solar cell structure and parameters, such as the a-Si:H passivation layer thicknesses (thicker i-a-Si:H layers shift the cut-off temperature of the peak in efficiency towards higher temperatures and reduce the overall efficiency of the cell [37], whereas the optimal thickness of the p-a-Si:H and n-a-Si:H layers depends on the i-a-Si:H layer used [38, 39]). Experimental measurements presented in Refs. 38 and 39 are added in Fig. 2(a) as crosses (grey) to validate the observed trends in simulated results of conversion efficiency. The same general trend in efficiency can be observed, however, some deviations can be noticed as the simulated cell was not fitted to the parameters of the measured one. Similar experimental trends with respect to the temperature have also been experimentally demonstra-

ted in Refs. 16 and 18. Referring to those publications, other solar cell parameters (FF , J_{SC} , and V_{OC}) follow the experimentally observed trends, as well.

The fill factor FF of the ideal ohmic case in Fig. 2(b) decreases steadily with increasing temperature, however, a significant decrease at lower temperatures is observed in the case with the ITO contacts. This decrease of FF at lower temperatures is the cause of the drop in efficiency in this temperature range. The highest FF of our simulated cell is $\sim 83\%$ at about 35°C . The values of FF at $T = -20^\circ\text{C}$ and 80°C are $\sim 64\%$ and $\sim 79.5\%$, respectively.

Continuing with the short-circuit current density in Fig. 2(c), it can be observed, considering the scale, that it changes much less than the other parameters (not more than 1 mA/cm^2 within the given temperature range) and, thus, has little effect on efficiency in both cases. A similar linear trend of increase in J_{SC} with increasing temperature can be observed for the cases of ideal ohmic and ITO contacts.

Finally, the open-circuit voltage temperature dependency is presented in Fig. 2(d). It can be observed that the V_{OC} drops almost linearly as temperature increases in both cases. This result shows that efficiency is governed by the reduction of V_{OC} and partially FF at temperatures $> 300\text{ K}$ (26.85°C).

In the presented simulations, the contacts on both sides were the same and were either ideal ohmic or ITO. As will be demonstrated later, the ITO/p-a-Si:H heterojunction is more critical and influences the efficiency of the cell more than the ITO/n-a-Si:H junction also in terms of temperature dependency.

3.2. Effects of ITO work function on temperature dependency of efficiency

Hereafter, only the realistic cell with the ITO contacts was considered in the analysis. It is known and can be also

observed in the energy band diagram in Fig. 1(b) that there is an inherent work function (WF) difference between the ITO and the doped a-Si:H layers (work function mismatch) which influences the efficiency of the cell even at 300 K (26.85°C). In order to investigate the role of WF of ITO layers and, consequently, work function mismatch with the doped a-Si:H layers on the performance of the SHJ cell at various temperatures, the electron affinity of the ITOs was varied. In this study, the WF of ITOs on each, p- and n-side separately, was varied while leaving the parameters of the ITO on the other side at their reference values. The doping density of ITO was kept at its reference level ($1 \cdot 10^{20}\text{ cm}^{-3}$) during this investigation and corresponds to a degenerately doped ITO with a 260 meV difference between the fermi level (E_F) and the conduction band (E_C). The chosen range of the work functions used in our analysis (4.2 eV – 5.2 eV) and corresponding electron affinities ($\chi = 4.46\text{ eV}$ – 5.46 eV) present different ITO contacts that can be manufactured and applied to real solar cells [40]. The individual WF values of ITOs, once set, have not been changed with temperature.

Efficiencies of the cells as a function of the temperature are presented in Fig. 3(a)–(b) for the variation of the WF of ITO at the p- and n-side, respectively. Differently coloured curves present simulations with ITOs including different work functions. The reference case, where ITOs are the same on both sides and their parameters are at the reference values, is presented by a full black line with a work function of $WF = 4.7\text{ eV}$ and an electron affinity of $\chi = 4.96\text{ eV}$.

By focusing first on Fig. 3(a), where the ITO work function was varied on the p-side, it was found out that higher work functions of ITO lead to a better efficiency over the entire temperature range. This general trend of increase is linked to the lowering of the work function mismatch between the ITO and p-a-Si:H [41]. Regarding the temperature dependency, it can be observed that

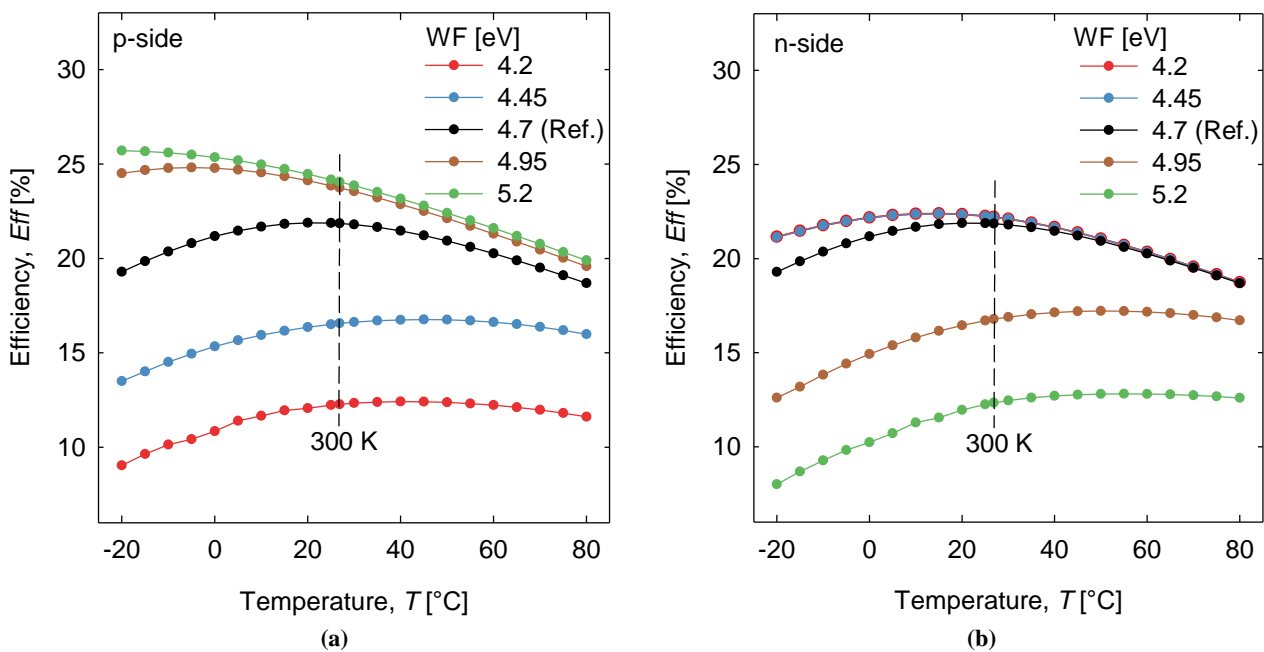


Fig.3. Efficiency vs. temperature for different ITO work functions (coloured lines) when variation is done only on the ITO adjacent to the p-a-Si:H (a), while the ITO parameters next to the n-a-Si:H are kept at their reference values and vice-versa (b). Vertical dashed line marks the reference temperature (300 K or 26.85°C). The reference case (Ref.), where both sides have the same reference ITO material, is presented by a black solid line.

efficiency changes much less when the temperature is increased above 300 K (26.85 °C) for all work functions presented here. Although not clearly visible in the presented temperature range, the temperature at which the maximum efficiency is achieved tends to shift toward higher temperatures as the work function is decreased.

It is also worth noting that increasing the work function above 4.95 eV (brown line) offers only a limited increase in efficiency even at lower temperatures. The highest work function of 5.2 eV (green line) almost eliminates the work function mismatch and yields very similar Eff and FF as the ideal ohmic case [white circle markers in Fig. 2(a) and 2(b)] at temperatures above 300 K (26.85 °C). At lower temperatures (< 300 K or 26.85 °C), however, it still performs worse, indicating possible transport issues across the heterointerfaces (ITO/a-Si:H and a-Si:H/c-Si).

The results where the work function of ITO was varied on the n-side, while the reference ITO was used on the p-side, are shown in Fig. 3(b). Here one can observe higher Eff values for the ITOs with a lower WF . This is because lower WF values of ITO decrease the work function mismatch between the ITO and n-a-Si:H in this case (just the opposite compared to the p-side). Also, in this case, the efficiency tends to change much less at temperatures above the reference (> 300 K or 26.85 °C) than at lower temperatures regardless of the WF value. The shift of maximum-efficiency temperature seems to move toward higher temperatures when ITO WF is increased on the n-side. Additionally, it can be observed that WF values of 4.2 eV (red line) and 4.45 eV (blue line) yield almost identical results, suggesting that the reference work function mismatch between the ITO and p-a-Si:H on the p-side already presents a bottleneck and mitigates the benefits of the variations at the n-side. This is also reinforced by the fact that work function mismatch between the ITO and n-a-Si:H on the n-side is almost entirely eliminated by employing an ITO with a WF of 4.2 eV in the presented case, yet it still yields lower efficiency at higher temperatures when compared to the ideal ohmic case from Fig. 2(a).

A detailed explanation of the observed effects will be addressed in the following section.

4. Discussion

The results shown in section 3 will now be discussed in more detail to explain the mechanisms that determine the temperature behaviour of the external parameters of the SHJ cell. First, all temperature dependencies as described in section 2.3 (assigned to cumulative effects) are taken into account, whereas in the second part of the discussion an attempt was made to de-couple these effects to identify which dependencies significantly affect the SHJ cell performance (analysis of individual effects).

4.1. Analysis of the cumulative effects of temperature-dependant parameters

Graphs in Fig. 2 show that the efficiency of the cell at lower temperatures (< 300 K or 26.85 °C) is mainly determined by the FF decrease, whereas the drop in V_{OC} determines and decreases the efficiency at higher temperatures (> 300 K or 26.85 °C). The efficiency of the

reference cell (21.86 %) is very close to the observed maximum (~21.9 %), as the decrease in FF is mitigated by the increase in V_{OC} at the reference temperature (300 K or 26.85 °C).

Focusing first on the decrease in V_{OC} ; the effect is well known and is not related to heterostructures per se [42]. Basic equations for an illuminated p-n junction show that the decrease in V_{OC} at increased temperature is related to increased intrinsic carrier concentration which affects minority carrier concentration in the doped layers [5, 43].

The increase in minority carriers also increases the activation energy [as per equations (1) and (2)] of the highly doped p-a-Si:H and n-a-Si:H layers which also decreases the difference between the WF energies between the two materials, resulting in a weaker built-in electric field that is needed for charge separation. Since free charges are not swiped out of the bulk as effectively, recombination increases in the n-c-Si bulk of the SHJ cell leading to a decrease in the V_{OC} . The opposite is true for low temperatures, where V_{OC} increases due to a WF difference and reduced recombination in the bulk as minority carrier concentrations are reduced.

Let us now focus on the decrease in FF at lower temperatures for the realistic SHJ cell with ITO contacts. It can be seen in the energy-band diagram presented in Fig. 1(b) that there are two i-a-Si:H/n-c-Si (encircled 1a and 2a) and two ITO/a-Si:H heterojunctions (encircled numbers 1 and 2, respectively.) in the reference device. Different electron affinities and band gap energies of the adjacent layers, forming the heterojunctions, create offsets in the valence and conduction bands. The offsets define the height of the energy barriers near the heterointerfaces that impede holes and electrons as they flow from the n-c-Si bulk, where they were optically generated, toward the cathode and the anode, respectively. Tunnelling mechanism (BBT, TAT, DT) and thermionic emission (TE) help the carriers cross such barriers and are crucial for the operation of the SHJ cell [15]. Tunnelling efficiency and TE decrease as temperature is lowered, leading to a reduction in FF , mostly due to transport issues at the ITO/a-Si:H interfaces, as confirmed by simulations. The drop in FF does not occur in the given temperature range when the ITO contacts are replaced with ideal ohmic boundary conditions, as the barriers at the ITO/a-Si:H interfaces were effectively removed. The remaining i-a-Si:H/n-c-Si heterointerfaces pose a bottleneck in transport at much lower temperatures (not shown here). Additional simulations also showed that when tunnelling is omitted at the i-a-Si:H/n-c-Si junctions, the reduction in TE at lower temperatures leads to poor FF even in the case of ideal ohmic contacts (also not shown here) in the presented temperature range.

It is worth noting here that the electron affinity of ITO not only determines the conduction and valence band offsets at the ITO/a-Si:H heterointerfaces, but also affects the work function mismatch: ΔWF (difference between the work functions of ITO and the adjacent a-Si:H layer). It was shown in our previous publication that a high ΔWF can degrade the electric field required for charge separation, if the adjacent a-Si:H layer is either too thin, insufficiently doped, or has too low density of defect states at energies near the Fermi level to screen the ITO charge [15]. The results in Fig. 3(a) where the electron affinity of ITO was

varied on the p-side, while keeping ITO on the n-side at the reference level, showed that increasing the WF above the reference value (4.7 eV) leads to significant improvements in FF (not shown here) and, consequently, in efficiency at lower temperatures, whereas at higher temperatures the effect is less pronounced. This is because a higher WF reduces the ΔWF between the ITO and p-a-Si:H and relaxes the constraints on screening of the positive ionized dopant charge (N_b^+) in the space-charge region (SCR) of ITO. As a result, a stronger electric field is formed in the bulk for charge separation. A stronger electric field mitigates the negative effect of a poor tunnelling efficiency at lower temperatures, as well as the negative effects of increasing barrier heights, since increasing the electron affinity also increases the conduction and valence-band offsets in this case. A similar explanation is proposed for the cases where the electron affinity of the ITO was lowered on the n-side, while keeping the reference values for the ITO on the other side which reduced the work function mismatch between ITO and n-a-Si:H. Moreover, lowering the ITO electron affinity on the n-side also reduced the conduction and valence-band offsets at the n-a-Si:H/ITO heterointerface, resulting in lower energy barriers. It can be observed that the increase in efficiency at lower temperatures is not as pronounced in this case as compared to the gains when ITO is optimized on the p-side. This is because the n-a-Si:H layer of the reference cell is more capable of screening the ITO charge than the p-a-Si:H layer due to a more favourable energetic distribution of defect states (for details refer to our previous publication [15]).

Delving further into detail, an investigation regarding the temperature effects related to the FF as a parameter defined by the product of the maximum-power-point current density (J_{MPP}) and voltage (V_{MPP}) divided by the product of J_{SC} and V_{OC} was performed. In Fig. 4 selected current-voltage or $J(V)$ curves corresponding to the SHJ solar cell operation at different temperatures are shown where the MPP points are clearly marked.

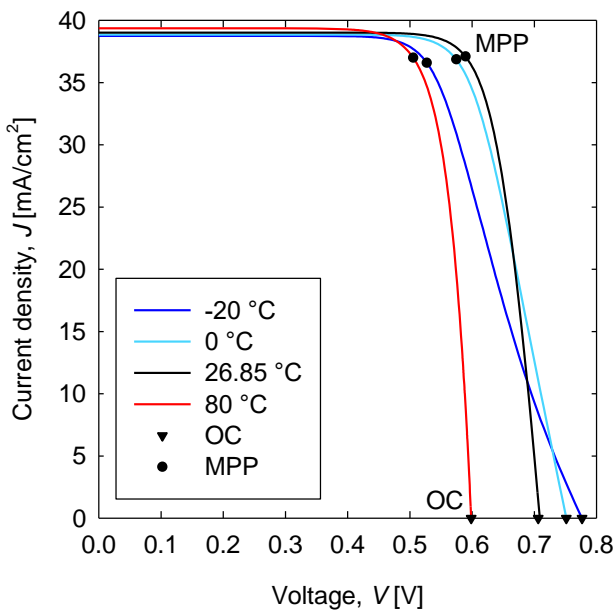


Fig. 4. Current-voltage characteristics of the reference cell at $-20\text{ }^\circ\text{C}$ (dark blue), $0\text{ }^\circ\text{C}$ (light blue), $26.85\text{ }^\circ\text{C}$ (black, reference), and $80\text{ }^\circ\text{C}$ (red). The MPP is marked with black dots and the open-circuit (OC) is marked with black triangles.

It can be observed that J_{SC} and J_{MPP} (corresponding to vertical position of MPPs on the graph) remain more or less unaffected at both high (red curve) and low temperatures (light and dark blue curves) and have only a minor impact on the FF change. At high temperatures (red curve) both V_{MPP} and V_{OC} decrease by roughly the same factor, resulting in minor changes of the FF (Fig. 2). Reasons behind the drop in V_{OC} at high temperatures have already been discussed where it was concluded that the increase of minority carriers leads to a weaker electric field, needed for charge separation. The weaker electric field also leads to a lower V_{MPP} .

At low temperatures, however, the V_{MPP} again decreases, but V_{OC} now increases (contrary to high temperatures) resulting in the observed drop of FF . It is also worth noting that the $J(V)$ curves start becoming S-shaped at lower temperatures (reduction in FF) which is also indicative of transport problems across the hetero-barriers [16, 44], leading to a low V_{MPP} despite the higher field for charge separation. The main difference between V_{OC} and V_{MPP} is that there is a significant current flowing across the cell at MPP conditions.

Mentioned transport limitations influence the charge distribution throughout the device, which, according to the Poisson's equation, affects the V_{MPP} and, consequently, FF and Eff . In order to explain this effect, the charge distribution at different temperatures was studied. The total charge (comprised of free charges, ionized dopants, and trapped charges due to defect states) and its distribution as a function of depth was obtained with simulations. This total charge across the depth of each layer was integrated into so-called sheet-charge, as shown in Fig. 5 to better represent the charge re-distribution when the reference temperature ($26.85\text{ }^\circ\text{C}$ or 300 K , black bar) is decreased to $-20\text{ }^\circ\text{C}$ or 253.15 K (dark blue bar). The comparison was made under MPP condition of the cell at almost identical J_{MPP} currents at both temperatures. It can be observed from Fig. 5 that there are differences in total sheet charge mostly

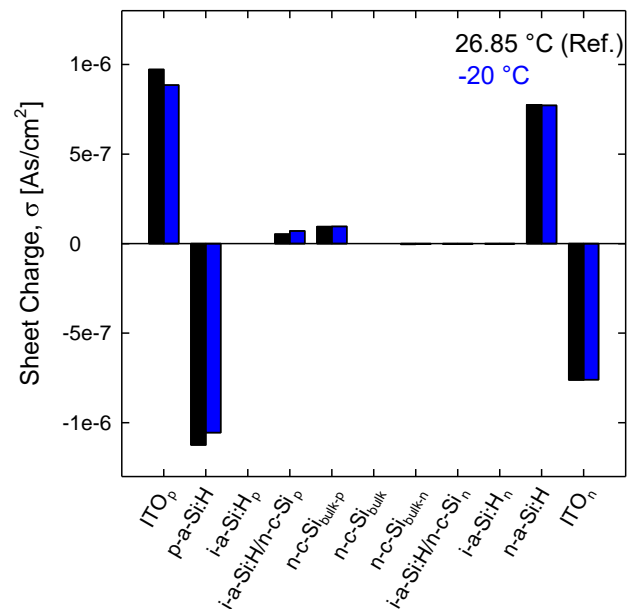


Fig.5. Total sheet charge for individual layers of the reference cell under the MPP condition at 300 K or $26.85\text{ }^\circ\text{C}$ (black, reference) and $-20\text{ }^\circ\text{C}$ (blue).

in the ITO on the p-side and in the p-a-Si:H layer. A reduction in positive total sheet charge in the ITO at lower temperatures and a decrease of negative charge in the p-a-Si:H can be observed. Also, in simulations it was observed that the reduction of positive charge in the ITO at low temperatures reflects poor transport of free electrons (which compensated the positive ionized N_D^+) out of the ITO as tunnelling efficiency is reduced. This observation is also directly linked to the decrease of negative charge in the p-a-Si:H which actually turned out to be an increase of positive charge due to vacant donor-like tail states as revealed by a detailed analysis of defect states, enabled by simulations. The donor-like tail states are positively charged when being vacant and become neutral only when occupied by an electron. The same is true for the +/0 Gaussian dangling bond states which are more or less completely vacant (they stay positively charged) at both temperatures, due to their energy distribution, positioning them at energies where the probability of occupancy by an electron is very low. It was demonstrated in our previous publication [15], according to the Poisson's equation, that a virtual shift of a positive charge from the layer close to the solar cell contact (front ITO in this case) towards the layer which is away from the contact, even for a few nano meters (p-a-Si:H in this case), leads to a reduction in the generated voltage and, consequently, to reduced efficiency while the current density remains approximately unchanged.

4.2. Analysis of individual effects of temperature-dependant parameters

The preceding section was dedicated to the cumulative effects of temperature-dependant parameters (described in section 2.3) on charge redistribution and, consequently, on voltage and, ultimately, on efficiency. Authors continue their research on the temperature effects, by looking at individual temperature-dependant parameters and their effect on the external performance parameters of the cell. The curve of the reference cell with ITO contacts is added where all temperature-dependant parameters are considered. During this analysis, the fundamental temperature dependency related to the thermal energy (kT) was considered in all presented cases, whereas other dependencies (N_C and N_V , E_G , χ , and μ) were added separately in the simulations as denoted in the legends of Fig. 6. Such de-coupled analysis also allows assigning the temperature trends observed in Fig. 2 to different temperature effects.

It can be generally observed that the temperature variation in the kT (orange curve) term alone already reproduces all the main temperature trends observed for almost all external parameters, except for the J_{SC} . This observation could be generalized also for other types of solar cells, since the kT product is a fundamental quantity that appears in physical models of devices. However, depending on a particular solar cell structure made of different semiconductor materials, resulting in different bulk and interface properties, other temperature dependencies may become more or less pronounced. Therefore, detailed research of optoelectronic mechanisms of individual cell structures is required to explain its particular realistic behaviour.

Focusing further on the J_{SC} behaviour of the analysed SHJ cell, it can be observed from Fig. 6(c) that the J_{SC} increases linearly with increasing temperature only when the changes in optical absorption due to temperature variation in the band gap are taken into account ($E_{G\text{ opt.}}$, green curve), as this line closely follows the reference case. In all other cases, the J_{SC} tends to slightly drop as temperature increases, presenting the opposite trend. However, it should be noted that the abscissa is zoomed in for J_{SC} and that the maximum span presented here is below 1 mA/cm².

Focusing now on the efficiency parameter, it can be seen in Fig. 6(a) that thermal energy (kT , orange) dominates the main temperature dependence, especially at lower temperature as it closely follows the reference curve. Same observation can be made for the FF , presented in Fig. 6(b). This is because the lowering of the kT product directly affects the capture and emission rates of the phonon-assisted [45] and elastic tunnelling [46] transitions of the TAT models and reduces tunnelling efficiency at these temperatures. At higher temperatures, however, a slight increase in efficiency compared to the reference curve when considering only the kT product can be observed.

By adding the mobility temperature dependency to the kT effects (brown curve), almost exactly the same efficiency values are obtained as for the kT (orange) curve in the entire temperature range. This implies that temperature-induced changes in mobility have only a minor influence on the device performance.

If the temperature dependences N_C and N_V are added to the kT effects (red curve), the efficiency at both low and high temperatures is a bit higher compared to the reference (black), whereas at lower temperatures it is also a bit higher than the kT (orange) curve. This low-temperature increase in efficiency is due to a slight increase in FF [Fig. 6(b)], whereas the increase at high temperatures is due to a slight increase in V_{OC} [Fig. 6(d)]. The observation regarding the FF can be explained by the fact that both N_C and N_V also decrease with decreasing temperature which results in even lower concentrations of minority carriers. This is reflected in a higher work function mismatch between the ITO and the p-a-Si:H layer [15]. Consequently, there is a higher tendency for electrons to travel from the ITO towards the p-a-Si:H where they neutralize more positive charge compared to the kT and the reference case. Note that the high work function mismatch generally leads to a poor FF when tunnelling is efficient, as electrons may travel too deep in the cell and weaken the electric field needed for charge separation. Even in this case, the V_{OC} is slightly weaker at lower temperatures compared to the kT and the reference case, reflecting the increase in the work function mismatch. The opposite is true at higher temperature. Tunnelling is now more efficient, and the work function mismatch is reduced as N_C and N_V are increased. This effect overpowers the increase of minority carrier concentrations resulting in a slight increase in V_{OC} at higher temperatures. This result implies that the inclusion of other temperature dependant parameters should decrease the efficiency, resulting in the reference curve (black).

The combination of kT and temperature dependence of the electrical band gap ($E_{G\text{ ele.}}$) and the electron affinity (χ), shown here in blue, reduces the efficiency over the entire temperature range compared to the reference curve (black).

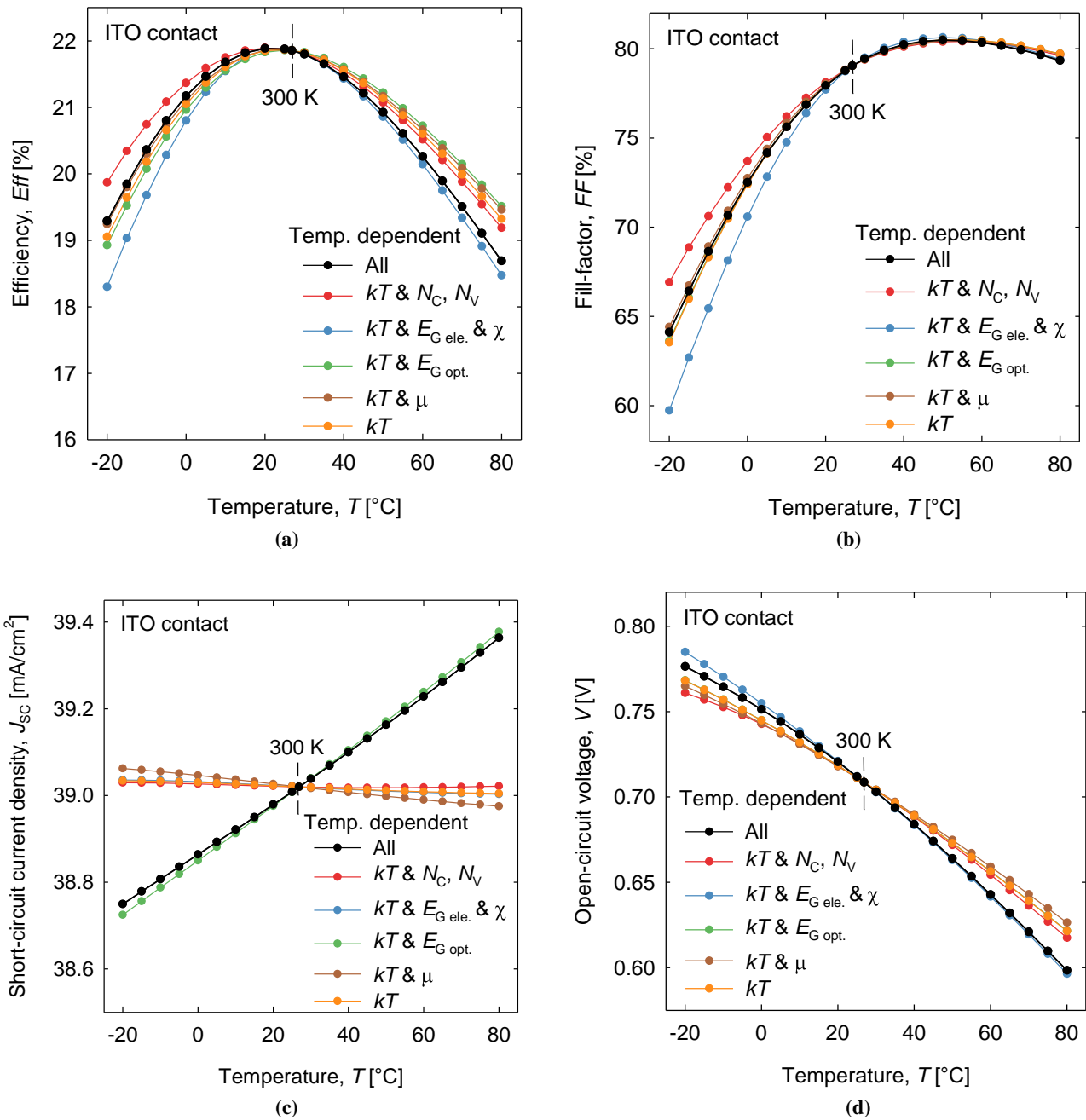


Fig. 6. Efficiency (a), fill factor (b), short-circuit current density (c), and open-circuit voltage (d) vs. temperature. The black full line presents the case where all temperature models (All) were enabled and is referred to a reference curve. The red line presents the cases where temperature dependency was enabled only for effective density of states for electrons and holes (kT and N_C, N_V). The blue line presents the cases where temperature dependency of both band gap and electron affinity was enabled, but its effect on optical absorption and carrier generation (kT and $E_{G\text{ ele.}} & \chi$) was excluded. The green line presents the cases where temperature dependency was enabled only for the optical absorption and free carrier generation (kT and $E_{G\text{ opt.}}$). The brown line presents the cases where temperature dependency of mobility (kT and μ) was enabled and the orange line presents the cases where only thermal energy changed with temperature (kT).

It should be noted that in this case the changes in the band gap were only included in the electrical simulations, i.e., the optical generation was calculated using the absorption in the reference case. The drop in efficiency (and FF) at lower temperatures is partly due to the wider band gap leading to larger differences between the ITO conduction-band edge and valence-band edge energies of the p-a-Si:H and, thus, lower tunnelling efficiency, in particular TAT and BBT [47], as well as the work function mismatch [28]. The electron affinity, which also changed in this case, was reduced by half the amount by which the band gap increased from the reference value according to equations

(6) and (7), partially offsetting the negative effects of the wider band gap by reducing the work function mismatch and bringing the valence-band edge of the p-a-Si:H closer to the conduction-band edge of the ITO. The wider band gap had little effect on the n-a-Si:H, but the reduction in electron affinity in the n-a-Si:H slightly increased the work function mismatch with the ITO and decreased the conduction-band offset which slightly increased direct tunnelling. High temperature behaviour in this case is not so different compared to the reference case, since it is only slightly lower due to the lower J_{SC} , as the absorption did not increase with temperature. Of note is also the observation

that the combination of kT , electrical band gap, and electron affinity governs the V_{OC} behaviour at high temperatures, since the blue and black curves are almost identical at these temperatures.

It seems that the temperature effects of N_C , N_V , $E_{G\text{ ele.}}$, and χ mitigate each other in the reference case which is especially evident at low temperatures ($< 300\text{ K}$ or $26.85\text{ }^\circ\text{C}$) as the reference curve (black) is almost midway between the red and blue curves. The same observation can be made for the FF in Fig. 6(b). At higher temperatures, however, the negative effects of $E_{G\text{ ele.}}$ and χ outweigh the beneficial effects of N_C and N_V .

Some generalization of the observations can be made to some extent, namely, in recent studies it was shown that V_{OC} determines the cell efficiency at higher temperatures due to the increase in the intrinsic carrier density (increased recombination) not only in conventional solar cell devices, but also in perovskite-based solar cells [48]. Further generalizations of the specific temperature dependencies and, especially, their influence on external characteristics could be made after a careful study of specific solar cell structures. The application of optoelectronic simulations and the approach presented in this work can be very helpful in such studies.

5. Conclusions

In this work, authors have performed the opto-electrical modelling of a SHJ solar cell, taking into account realistic ITO layers with associated tunnelling mechanisms (DT, TAT, and BBT). The model for studying the effect of temperature variations on the external performance parameters of the cell in the range from $-20\text{ }^\circ\text{C}$ to $80\text{ }^\circ\text{C}$ was chosen. The effect of the contact WF in relation to temperature variations was also investigated. A detailed study of the effects of individual temperature-dependent material parameters (optical and electrical band gap, electron affinity, thermal energy, mobility, and effective density of states in the conduction and valence bands) on the performance was also carried out.

The behaviour of the cell at temperatures lower than 300 K ($26.85\text{ }^\circ\text{C}$) has been shown to be governed by a drop in FF due to transport problems, as the tunnelling efficiency is reduced, which was also confirmed by the S-shaped $J(V)$ curves at these temperatures. This drop in FF was associated with a decrease in MPP voltage. It has been shown that the voltage drop at lower temperatures is a consequence of a poor tunnelling of electrons flowing from ITO towards p-a-Si:H. This led to a decrease in the positive charge in ITO and an increase in the positive charge in the p-a-Si:H layer, as fewer electrons were now available to mitigate the positively charged (vacant) donor-like trap states in p-a-Si:H. Poor tunnelling is, thus, reflected in the virtual shift of the positive charge from ITO to the p-a-Si:H, leading to a low MPP voltage according to the Poisson's equation. Moreover, it has been shown that the thermionic emission plays a significant role at low temperatures only in the absence of tunnelling mechanisms.

However, at temperatures higher than 300 K ($26.85\text{ }^\circ\text{C}$), a decrease in V_{OC} plays a crucial role because the concentration of minority carriers is higher, leading to a smaller difference in the work function between the p- and

n-side of the device, which translates into a lower electric field required for charge separation. In comparison, the FF changed much less at high temperatures.

It has been demonstrated that the ITO WF has a large effect on the temperature response of the cell due to the work function mismatch. Authors have also shown that a high electron affinity on the p-side reduces mismatch and provides high efficiency gains, especially at low temperatures, while lowering the electron affinity on the n-side reduces mismatch but provides limited efficiency gains over the entire temperature range. Moreover, it was demonstrated that the ITO/p-a-Si:H junction determines the cell temperature behaviour more than the n-a-Si:H/ITO junction, because the work function mismatch has a larger impact since the trap distribution in the p-a-Si:H layer is less favourable than in the n-a-Si:H. Consequently, the effect of poor tunnelling is more pronounced at the ITO/p-a-Si:H junction, leading to tighter constraints on the work function mismatch.

Regarding the effects of the individual temperature-dependant parameters, it has been shown that the overall behaviour of the cell temperature depends on the thermal energy (kT), while other parameters have little effect on the device. It was also found that the low temperature behaviour of the cell is determined by the variations of kT , N_C , and N_V , which mitigate the effects of the variation of χ and $E_{G\text{ ele.}}$. Also, it was observed that the linear increase in J_{SC} with increasing temperature is a consequence of the increased optical absorption. The mere electrical band gap narrowing causes the opposite trend, therefore, it is mandatory to take into account both optical and electrical band gap variations in order to correctly simulate the device.

The presented results offer an insight into the temperature behaviour of the SHJ cells and their components and can serve as a guide for further optimization of the cells operating at various temperatures in different climatic zones.

Authors' statement

Research concept and design, J. Krč and J. Balent; collection and/or assembly of data, J. Balent; data analysis and interpretation, J. Balent; writing the article, J. Balent, J. Krč; critical revision of the article, M. Topič and J. Krč; final approval of article, J. Krč and M. Topič.

Acknowledgements

The authors acknowledge the financial support from the Slovenian Research Agency-ARRS (program P2-0197 and PhD funding for J.B.). The authors would also like to thank Dr Mathieu Boccard from EPFL PV-LAB, Neuchatel, Switzerland, for the useful experimental indications which inspired this work.

References

- [1] Green, M. *et al.* Solar cell efficiency tables (version 57). *Prog. Photovolt.* **29**, 3–15 (2021). <https://doi.org/10.1002/pip.3371>
- [2] Langner, A. Photovoltaics Report. *ise.fraunhofer* <https://www.ise.fraunhofer.de/content/dam/ise/de/documents/publications/studies/Photovoltaics-Report.pdf>. (2021). (Accessed: 8th Nov. 2021).

- [3] Battaglia, C., Cuevas, A. & De Wolf, S. High-efficiency crystalline silicon solar cells: status and perspectives. *Energy Environ. Sci.* **9**, 1552–1576 (2016). <https://doi.org/10.1039/C5EE03380B>
- [4] Feldmann, F., Reichel, M. B. C., Hermle, M. & Glunz, S. W. A Passivated Rear Contact for High-Efficiency n-Type Silicon Solar Cells Enabling High Vocs and FF>82%. in *28th European Photovoltaic Solar Energy Conference and Exhibition 988–992* (2013). <https://doi.org/10.4229/28thEUPVSEC2013-2CO.4.4>
- [5] Luque, A. & Hegedus, S. *Handbook of Photovoltaic Science and Engineering*. (John Wiley & Sons, Ltd., 2011).
- [6] Yamaguchi, M., Dimroth, F., Geisz, J. F. & Ekins-Daukes, N. J. Multi-junction solar cells paving the way for super high-efficiency. *J. Appl. Phys.* **129**, 240901 (2021). <https://doi.org/10.1063/5.0048653>
- [7] Best Research-Cell Efficiency Chart. *National Renewable Energy Laboratory* <https://www.nrel.gov/pv/cell-efficiency.html> (Accessed: 27th Dec. 2021).
- [8] Yoshikawa, K. *et al.* Silicon heterojunction solar cell with interdigitated back contacts for a photoconversion efficiency over 26%. *Nat. Energy* **2**, 17032 (2017). <https://doi.org/10.1038/nenergy.2017.32>
- [9] Richter, A., Hermle, M. & Glunz, S. W. Reassessment of the limiting efficiency for crystalline silicon solar cells. *IEEE J. Photovolt.* **3**, 1184–1191 (2013). <https://doi.org/10.1109/JPHOTOV.2013.2270351>
- [10] Jaeckel, B. *et al.* Combined Standard for PV Module Design Qualification and Type Approval: New IEC 61215 - Series. in *29th European PV Solar Energy Conference and Exhibition (EU PVSEC 2014)* (2014).
- [11] Cattin, J. *et al.* Optimized design of silicon heterojunction solar cells for field operating conditions. *IEEE J. Photovolt.* **9**, 1541–1547 (2019). <https://doi.org/10.1109/JPHOTOV.2019.2938449>
- [12] Synopsys. Sentaurus™ Device User Guide Q-2020.09-SP1. (2020).
- [13] Cotfas, D. T., Cotfas, P. A. & Machidon, O. M. Study of temperature coefficients for parameters of photovoltaic cells. *Int. J. Photoenergy* **2018**, 5945602 (2018). <https://doi.org/10.1155/2018/5945602>
- [14] Dupré, O., Vaillon, R. & Green, M. A. *Thermal Behavior of Photovoltaic Devices: Physics and Engineering*. (Springer, 2016).
- [15] Balent, J., Smole, F., Topic, M. & Krc, J. Numerical analysis of selective ito/a-si:h contacts in heterojunction silicon solar cells: effect of defect states in doped a-si:h layers on performance parameters. *IEEE J. Photovolt.* **11**, 634–647 (2021). <https://doi.org/10.1109/JPHOTOV.2021.3063019>
- [16] Mikolášek, M., Racko, J. & Harmatha, L. Analysis of low temperature output parameters for investigation of silicon heterojunction solar cells. *Appl. Surf. Sci.* **395**, 166–171 (2017). <https://doi.org/10.1016/j.apsusc.2016.04.023>
- [17] Ganji, J. Numerical simulation of thermal behavior and optimization of a-Si/a-Si/C-Si/a-Si/A-Si hit solar cell at high temperatures. *Electr. Eng. Electromech.* **6**, 47–52 (2017). <https://doi.org/10.20998/2074-272X.2017.6.07>
- [18] Martini, L., Serenelli, L., Menchini, F., Izzi, M. & Tucci, M. Silicon heterojunction solar cells toward higher fill factor. *Prog. Photovolt.* **28**, 307–320 (2020). <https://doi.org/10.1002/pip.3241>
- [19] Heidarzadeh, H. Performance analysis of an HJ-IBC silicon solar cell in ultra-high temperatures: possibility of lower reduction efficiency rate. *Silicon* **12**, 1369–1377 (2020). <https://doi.org/10.1007/s12633-019-00230-5>
- [20] Abdallah, A. *et al.* Towards an optimum silicon heterojunction solar cell configuration for high temperature and high light intensity environment. *Energy Procedia* **124**, 331–337 (2017). <https://doi.org/10.1016/j.egypro.2017.09.307>
- [21] Krč, J., Smole, F. & Topic, M. One-dimensional semi-coherent optical model for thin film solar cells with rough interfaces. *Inform. MIDEM* **32**, 6–13 (2002). [http://www.midem-drustvo.si/Journal%20papers/MIDEM_32\(2002\)1p6.pdf](http://www.midem-drustvo.si/Journal%20papers/MIDEM_32(2002)1p6.pdf)
- [22] Lokar, Z. *et al.* Coupled modelling approach for optimization of bifacial silicon heterojunction solar cells with multi-scale interface textures. *Opt. Express* **27**, A1554–A1568 (2019). <https://doi.org/10.1364/OE.27.0A1554>
- [23] Holman, Z. C. *et al.* Current losses at the front of silicon heterojunction solar cells. *IEEE J. Photovolt.* **2**, 7–15 (2012). <https://doi.org/10.1109/JPHOTOV.2011.2174967>
- [24] Holman, Z. C. *et al.* Infrared light management in high-efficiency silicon heterojunction and rear-passivated solar cells. *J. Appl. Phys.* **113**, 013107 (2013). <https://doi.org/10.1063/1.4772975>
- [25] Palik, E. D. *Handbook of Optical Constants of Solids*. (Academic Press, Elsevier, 1997).
- [26] Kanevce, A. & Metzger, W. K. The role of amorphous silicon and tunnelling in heterojunction with intrinsic thin layer (HIT) solar cells. *J. Appl. Phys.* **105**, 094507 (2009). <https://doi.org/10.1063/1.3106642>
- [27] Procel, P. Opto-electrical modelling and optimization study of a novel IBC c-Si solar cell. *Prog. Photovolt.* **25**, 452–469 (2017). <https://doi.org/10.1002/pip.2874>
- [28] Procel, P., Yang, G., Isabella, O. & Zeman, M. Theoretical evaluation of contact stack for high efficiency IBC-SHJ solar cells. *Sol. Energy Mater. Sol. Cells* **186**, 66–77 (2018). <https://doi.org/10.1016/j.solmat.2018.06.021>
- [29] Shu, Z., Das, U., Allen, J., Birkmire, R. & Hegedus, S. Experimental and simulated analysis of front versus all-back-contact silicon heterojunction solar cells: effect of interface and doped a-Si:H layer defects. *Prog. Photovolt.* **23**, 78–93 (2015). <https://doi.org/10.1002/pip.2400>
- [30] Richter, A., Glunz, S. W., Werner, F., Schmidt, J. & Cuevas, A. Improved quantitative description of Auger recombination in crystalline silicon. *Phys. Rev. B* **86**, 165202 (2012). <https://doi.org/10.1103/PhysRevB.86.165202>
- [31] Filipic, M., Smole, F. & Topic, M. Optimization of Interdigitated Back Contact Geometry in Silicon Heterojunction Solar Cell. in *14th International Conference on Numerical Simulation of Optoelectronic Devices (NUSOD 14)* 161–162 (2014). <https://doi.org/10.1109/NUSOD.2014.6935406>
- [32] Lombardi, C., Manzini, S., Saporito, A. & Vanzi, M. A physically based mobility model for numerical simulation of nonplanar devices. *IEEE T. Comput. Aid. D.* **7**, 1164–1171 (1988). <https://doi.org/10.1109/43.9186>
- [33] Bludau, W., Onton, A. & Heinke, W. Temperature dependence of the band gap of silicon. *J. Appl. Phys.* **45**, 1846–1848 (1974). <https://doi.org/10.1063/1.1663501>
- [34] Riesen, Y., Stuckelberger, M., Haug, F.-J., Ballif, C. & Wyrsh, N. Temperature dependence of hydrogenated amorphous silicon solar cell performances. *J. Appl. Phys.* **119**, 044505 (2016). <https://doi.org/10.1063/1.4940392>
- [35] Tauc, J. Optical properties and electronic structure of amorphous Ge and Si. *Mater. Res. Bull.* **3**, 37–46 (1968). [https://doi.org/10.1016/0025-5408\(68\)90023-8](https://doi.org/10.1016/0025-5408(68)90023-8)
- [36] Zanatta, A. R. Revisiting the optical band gap of semiconductors and the proposal of a unified methodology to its determination. *Sci. Rep.* **9**, 11225 (2019). <https://doi.org/10.1038/s41598-019-47670-y>
- [37] Taguchi, M., Maruyama, E. & Tanaka, M. Temperature dependence of amorphous/crystalline silicon heterojunction solar cells. *Jpn. J. Appl. Phys.* **47**, 814–818 (2008). <https://doi.org/10.1143/JJAP.47.814>
- [38] Cattin, J. Influence of the Thicknesses of The Amorphous Silicon Layers on The Efficiency of Silicon Heterojunction Solar Cells for Various Climates. in *27th International Photovoltaic Science and Engineering Conference (PVSEC-27)* (2017). <https://pvsec-27.com/wp-content/themes/pvsec27/abstract/pages/abst/10389.pdf>
- [39] Cattin, J. Characterisation of Silicon Heterojunction Solar Cells Beyond Standard Test Conditions. (École polytechnique fédérale de Lausanne, 2020).
- [40] Klein, A. *et al.* transparent conducting oxides for photovoltaics: manipulation of fermi level, work function and energy band alignment. *Materials* **3**, 4892–4914 (2010). <https://doi.org/10.3390/ma3114892>
- [41] Bivour, M., Schröer, S. & Hermle, M. Numerical analysis of electrical TCO / a-Si:H(p) contact properties for silicon heterojunction solar cells. *Energy Procedia* **38**, 658–669 (2013). <https://doi.org/10.1016/j.egypro.2013.07.330>
- [42] Bivour, M. *Silicon heterojunction solar cells: Analysis and basic understanding*. (Fraunhofer Verlag, Freiburg, 2017).
- [43] Sachenko, A. V. *et al.* The temperature dependence of the characteristics of crystalline-silicon-based heterojunction solar cells. *Tech. Phys. Lett.* **42**, 313–316 (2016). <https://doi.org/10.1134/S1063785016030305>
- [44] Saive, R. S-shaped current–voltage characteristics in solar cells: A Review. *IEEE J. Photovolt.* **9**, 1477–1484 (2019). <https://doi.org/10.1109/JPHOTOV.2019.2930409>
- [45] Palma, A., Godoy, A., Jiménez-Tejada, J. A., Carceller, J. E. & López-Villanueva, J. A. Quantum two-dimensional calculation of time constants of random telegraph signals in metal-oxide-

- semiconductor structures. *Phys. Rev. B* **56**, 9565–9574 (1997). <https://doi.org/10.1103/PhysRevB.56.9565>
- [46] Jiménez-Molinos, F., Gámiz, F., Palma, A., Cartujo, P. & López-Villanueva, J. A. Direct and trap-assisted elastic tunneling through ultrathin gate oxides. *J. Appl. Phys.* **91**, 5116–5124 (2002). <https://doi.org/10.1063/1.1461062>
- [47] Procel, P. *et al.* The role of heterointerfaces and subgap energy states on transport mechanisms in silicon heterojunction solar cells. *Prog. Photovolt.* **28**, 935–945 (2020). <https://doi.org/10.1002/pip.3300>
- [48] Lin, L. & Ravindra, N. M. Temperature dependence of CIGS and perovskite solar cell performance: an overview. *SN Appl. Sci.* **2**, 1361 (2020). <https://doi.org/10.1007/s42452-020-3169-2>